RESEARCH ARTICLE

THE PROTEIN SOCIETY WILEY

Evolution of fungal tuberculosis necrotizing toxin (TNT) domain-containing enzymes reveals divergent adaptations to enhance NAD cleavage

Eugenio Ferrario[1] | **Juha Pekka Kallio**[1] | **Mahdi Emdadi**[1] |
Øyvind Strømland[1] | **Johannes G. M. Rack**[2] | **Mathias Ziegler**[1]

[1]Department of Biomedicine, University of Bergen, Bergen, Norway

[2]MRC Centre for Medical Mycology, University of Exeter, Exeter, UK

Correspondence
Mathias Ziegler, University of Bergen, Jonas Lies vei 91, 5009, Bergen, Norway.
Email: mathias.ziegler@uib.no

Review Editor: Lynn Kamerlin

Abstract

Tuberculosis necrotizing toxin (TNT) is a protein domain discovered on the outer membrane of *Mycobacterium tuberculosis* (*Mtb*), and the fungal pathogen *Aspergillus fumigatus*. TNT domains have pure NAD(P) hydrolytic activity, setting them apart from other NAD-cleaving domains such as ADP-ribosyl cyclase and Toll/interleukin-1 receptor homology (TIR) domains which form a wider set of products. Importantly, the *Mtb* TNT domain has been shown to be involved in immune evasion via depletion of the intracellular NAD pool of macrophages. Therefore, an intriguing hypothesis is that TNT domains act as "NAD killers" in host cells facilitating pathogenesis. Here, we explore the phylogenetic distribution of TNT domains and detect their presence solely in bacteria and fungi. Within fungi, we discerned six TNT clades. In addition, X-ray crystallography and AlphaFold2 modeling unveiled clade-specific strategies to promote homodimer stabilization of the fungal enzymes, namely, Ca^{2+} binding, disulfide bonds, or hydrogen bonds. We show that dimer stabilization is a requirement for NADase activity and that the group-specific strategies affect the active site conformation, thereby modulating enzyme activity. Together, these findings reveal the evolutionary lineage of fungal TNT enzymes, corroborating the hypothesis of them being pure extracellular NAD (eNAD) cleavers, with possible involvement in microbial warfare and host immune evasion.

KEYWORDS
actinomycetes, Ascomycota, extracellular NAD, *Fusarium oxysporum*, homodimer stabilization, host defense, NADase, *Neurospora crassa*, plant immunity
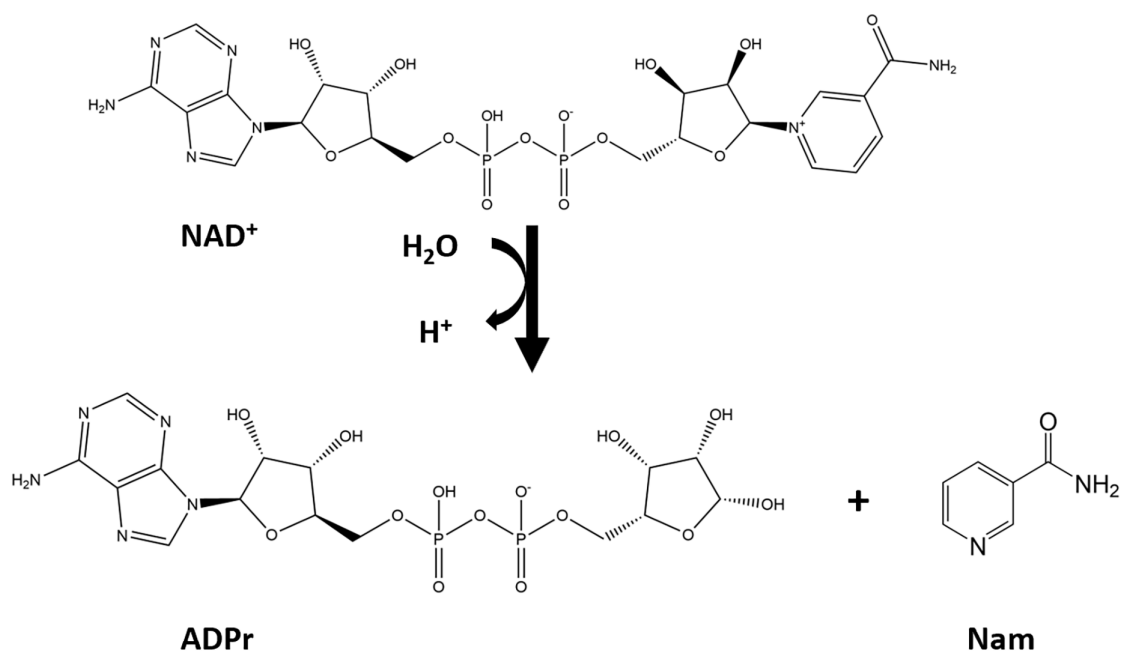
1 | INTRODUCTION

The pathogenic mechanism of the tuberculosis necrotizing toxin (TNT) from *Mycobacterium tuberculosis* (*Mtb*) has been demonstrated to be based on its catalytic activity as an NAD glycohydrolase (Figure 1a) (Danilchanka et al., 2014; Sun et al., 2015). In a recent study, we discovered NADase activity on the surface of another
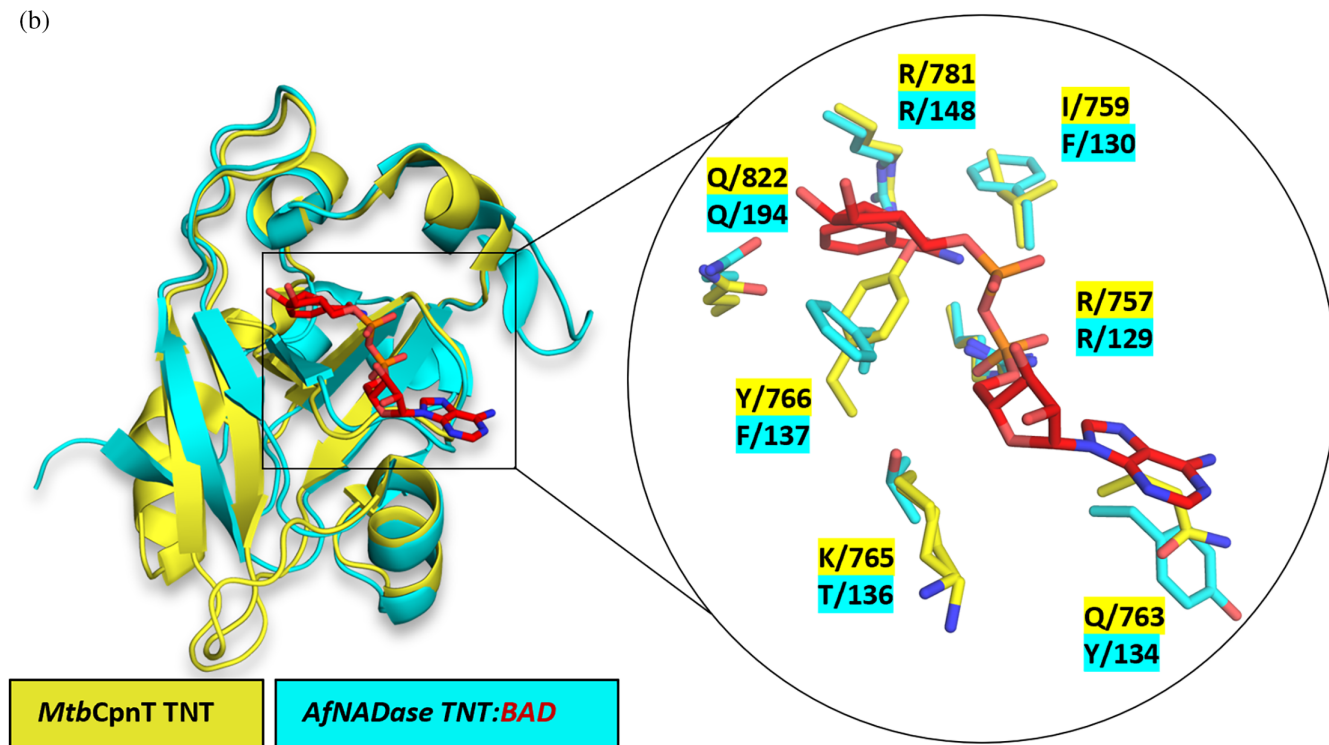
(a)

(b)

FIGURE 1 TNT domain NAD(P)$^+$ glycohydrolase activity. (a) Reaction scheme of TNT domain catalyzed NAD$^+$ glycohydrolysis: NAD$^+$ is cleaved utilizing a water molecule thus yielding nicotinamide (Nam) and adenosine diphosphate ribose (ADPr). (b) Superimposition of *Mtb*CpnT TNT domain (yellow, PDB 4QLP) with the TNT domain of *Af*NADase complexed with benzamide adenine dinucleotide (BAD) (turquoise/red, PDB 6YGG). In red the NAD substrate analog benzamide adenine dinucleotide bound in the active site of *Af*NADase. The magnification highlights the residues involved in substrate binding and catalysis (shown in sticks).

deleterious pathogen, the fungus *Aspergillus fumigatus* (Strømland et al., 2021). The causative protein was identified, and functionally and structurally characterized,

which led to the recognition that the catalytic domain is also of the TNT family albeit highly divergent, thus suggesting a common evolutionary origin (Figure 1b). A

peculiar trait of the TNT domain is its exclusive NAD hydrolase activity, and the lack of adenosine diphosphate ribose (ADPr) cyclase activity. This feature sets it apart from other NAD cleaving domains that additionally catalyze a cyclization reaction leading to the formation of cyclic ADP-ribose, cADPr (Essuman et al., 2017; Essuman et al., 2018). Indeed, the only known function of the TNT domain derives from studies of *Mtb*'s channel protein harboring the necrosis-inducing toxin (*Mtb*CpnT) domain at its C-terminus. The TNT domain of *Mtb*CpnT is exposed on the outer surface of the bacterium (Pajuelo et al., 2021). When internalized by macrophages, *Mtb* has the capability to breach the phagosomal membrane, thus gaining access to the macrophage's cytosol (Mittal et al., 2018; Simeone et al., 2012). Within this intracellular environment, *Mtb* employs its TNT domain to cleave the cellular NAD reservoir. Thereby, this enzymatic activity rapidly depletes the cellular NAD reservoir, ultimately leading to macrophage necrosis and facilitating immune evasion by the pathogen (Sun et al., 2015). Thus, *Mtb*CpnT has been categorized as the first known exotoxin of *Mtb*.

The identification of an extracellular NADase containing a TNT domain in *A. fumigatus* (*Af*NADase), has prompted the hypothesis that *Af*NADase may have a function analogous to that of the *Mtb*CpnT TNT domain. However, several distinctions exist between these two enzymes: before secretion, the TNT domain of *Mtb*CpnT is situated intracellularly and it is subject to inhibition by the immunity factor for TNT (IFT) protein. IFT protects the bacteria from depletion of its own NAD pool. Thus, in this inactive state, the TNT domain exists as a heterodimer (Sun et al., 2015). In contrast, *A. fumigatus* lacks a homolog of the IFT, and the pathway through which *Af*NADase reaches the cell exterior involves the secretory pathway, which would protect the cytosol from its catalytic activity. Sequence comparisons have indicated that there are other species in both the bacterial domain and the fungal kingdom that harbor TNT-encoding genes (Strømland et al., 2021). However, a comprehensive analysis of the phylogenetic distribution of TNT domain proteins is lacking and their occurrence in fungi and bacteria has not been systematically studied.

*Af*NADase exists as a homodimer (Strømland et al., 2021) and the two protomers are associated in a head-to-tail configuration, that is, the N-terminus of one protomer is in close vicinity to the C-terminus of the other protomer. The stability of the dimer is intricately regulated by a calcium ion binding motif located at the dimerization interface between the two protomers. Remarkably, the Ca^{2+} binding motif also governs the enzyme's turnover rate, via a long-range network of interactions that influence the active site's conformation upon Ca^{2+} binding or release (Ferrario et al., 2023). In this regard, it is surprising that the Ca^{2+} binding motif appears to be a unique trait in the order of Eurotiales (containing Aspergillus species) (Strømland et al., 2021), while, according to initial sequence comparisons, the structures of fungal NADases in other orders would be predicted to be otherwise highly similar. Given the functional importance of this motif in *Af*NADase, its predicted absence in other fungal NADases is puzzling.

In the present study, we analyzed the phylogenetic distribution of the TNT domain and its inhibitor IFT. The emergence of a fungi-specific TNT clade explains the high degree of sequence homology within fungi and the clear differences with bacterial TNT sequences. Using x-ray crystallography, AlphaFold2-based modeling, and biochemical assays, we revealed that three distinct strategies have evolved in fungi to maintain the homodimeric configuration of the ecto-NADase. Moreover, we show that these mechanisms are crucial to preserve NAD hydrolase activity. These strategies not only promote dimer stabilization but also facilitate the adoption of an active site conformation similar to what was previously observed in the *Af*NADase, thereby modulating enzyme activity. These observations have thus revealed an unexpected evolutionary convergence leading to homodimer stabilization and activity enhancement of the NAD hydrolyzing domains, suggesting a strong evolutionary advantage of robust extracellular NAD cleavage activity.

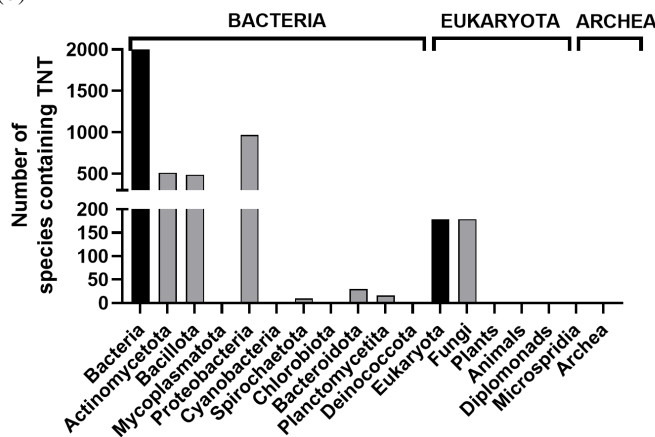## 2 | RESULTS

2.1 | Phylogenetic distribution of TNT-domains

The extracellular portion containing the TNT domain of *Mtb*CpnT (residues 653–846) and *Af*NADase display sequence similarities (Figure 2a). However, previous structural analyses of *Af*NADase (Ferrario et al., 2023) revealed characteristic regulatory features that are absent in the *Mtb* toxin. *Af*NADase contains an N-terminal signal peptide that mediates its secretion, a C-terminal Ca^{2+} binding motif, and an active site ^{156}NTFDGMYFY^{162} accessory loop (Figure 2a). The latter two are involved in calcium-mediated homodimer stabilization and activity regulation (Ferrario et al., 2023). However, the substrate binding residues (Figures 1b and 2a) are either conserved or retain the same biochemical proprieties (aromatic group, hydrophobic side chain). Therefore, it would appear that *Af*NADase underwent a regulatory diversification while conserving the key residues involved in catalysis to maintain NAD hydrolase activity, suggesting an evolutionary gap between the two proteins. To
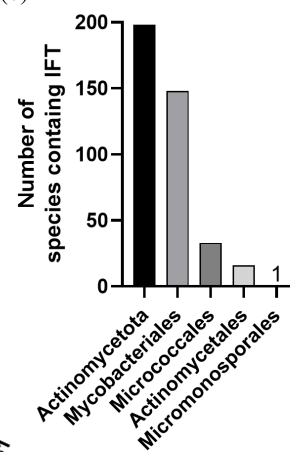
(a)

```
MtbCpnT CTerm  -----------RLSDEAVDPQY---GEPLSRHWDF-------T--DNPADRSRINPVVA   686
AfNADase       MIFTNAILVISALLPATVLSLQHTEDSLFPARCWPDPCAGITFQNDTYVCGDPRLGPVVL   60

MtbCpnT CTerm  QLMEDPNAPFGRDPQGQPYTQ-ERYQERFNS------VGPWGQQY----SNFPPNNGAV   734
AfNADase       P------------QKFPLNNELRTYARFGALCPAEFLDKWATDVAPNGTYIYPPANGFA   107

MtbCpnT CTerm  PGTRIAYTNLEKFLSDYGPQLDRIGGDQGKYLAIMEHGRPASWEQRALHVTSLR------   788
AfNADase       LDTEE-QPILGNATLPVGMKLDRFGSEYGTFLAPLGAP----YIERSLPPSNLNTFDGMY   162

MtbCpnT CTerm  -DPYHAYTIDWLPEGWFIEVSEVAPGCGQPGGSICVRIFDHQNEMRKVEELIRRGVLRQ-   846
AfNADase       PYNYHVYQ---VTKEFVVGLGPIAPWFEQPGMGTCFVTYT------NVLGLIDDGYLRRL   213

MtbCpnT CTerm  --------------------   846
AfNADase       DESEYDEKVEYSNPYTPGPN   233
```

| ▓ Signal Peptide | ▓ NAD binding | ▓ Ca²⁺ binding motif | ▓ ¹⁵⁶NTFDGMYPY¹⁶⁴ loop |

(b)

(c)

(d)

TAXA
- Eurotiomycetes
- Leotiomycetes
- Mortierellomycotina
- Sordariomycetes
- Dothideomycetes
- Agaricomycetes
- Mucoromycotina
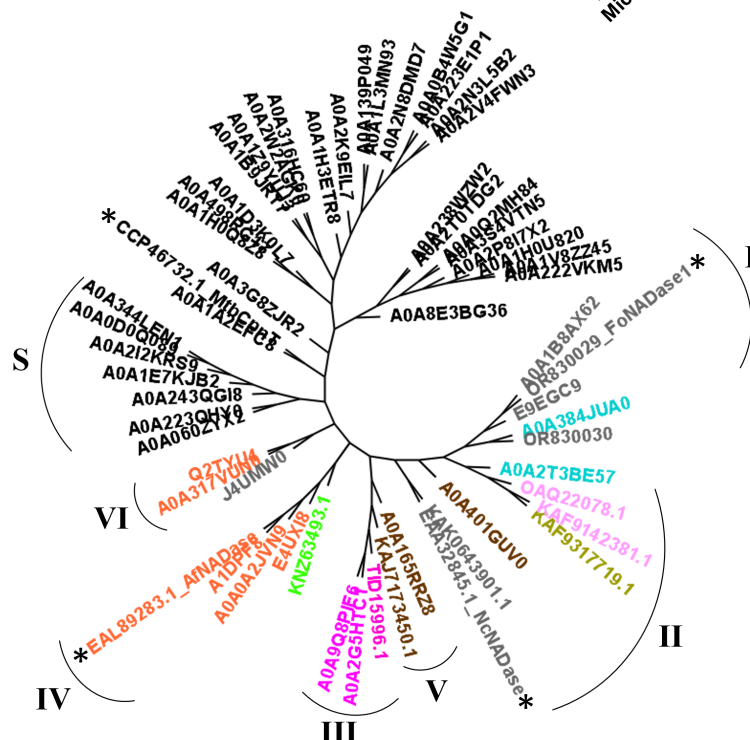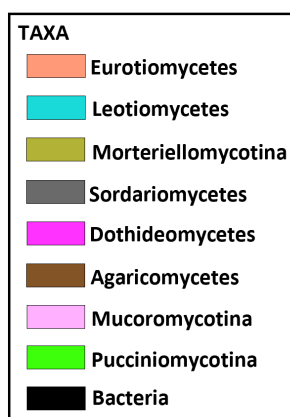- Pucciniomycotina
- Bacteria

FIGURE 2 Legend on next page.

determine the overall occurrence of TNT domains across the domains of life, we performed a BLAST search using the sequence of *Af*NADase TNT domain as the query sequence. The results of the analysis are shown in Figure 2b. The presence of TNT domains was detected in bacteria and eukaryotes. In bacteria, most hits were found in Actinomycetota, Bacillota and Proteobacteria. In eukaryotes, the TNT domain was detected exclusively in the fungal kingdom, with no indication of its existence in microorganisms such as protists or fungal-like oomycetes. According to our analyses, archaea completely lack TNT domain containing proteins.

BLAST searches performed with the interacting residues of the immunity factor IFT with *Mtb*CpnT revealed its presence solely in the Actinomycetota phylum, mostly in the Mycobacteriales order (Figure 2c), which includes *Mtb*. Consequently, in other bacterial phyla and fungi harboring TNT-proteins, alternative strategies to prevent self-toxicity may have evolved. As depicted in the phylogenetic tree (Figure 2d, Table S1 and S2), the distribution of the fungal TNT domains diverges from the bacteria phyla, with the closest bacterial clade formed mostly by Streptomyces (Clade S). Importantly, in a more comprehensive phylogenetic tree including 460 bacterial and fungal sequences, the distribution of fungal TNT-proteins diverges from the bacteria phyla with the exception of Streptomyces. The latter distributes between their own clade (Clade S) and Clade VI, which is shared with TNT-proteins from some members of the Aspargillaceae family (the phylogenetic tree can be accessed via GitHub depository link: https://github.com/UiBNAD/TNT_NADase). It is noteworthy that bacterial members of Clade S carry a predicted N-terminal signal peptide, otherwise uniquely found in fungal TNT-proteins. It was shown that bacteria inhabiting the same ecological niche as fungi, regularly engage in interspecies interaction (Marcet-Houben & Gabaldon, 2010), and therefore represent plausible candidates for horizontal gene transfer events, which may involve the TNT domain. Moreover, the presence of evolutionary distant fungal classes (Choi & Kim, 2017) mixed in the same clade, as visible in Clade II (Sordariomycetes, Morteriellomycotina,

Mucoromycotina, Leotiomycetes and Agaricomycetes), as well as the presence of Leotiomycetes in both Clades I and II, could be an indication for horizontal gene transfer events within the fungal kingdom. The *Mtb*CpnT protein is part of a separate, larger clade within bacteria.

2.2 | N/C-termini dictate the diversification of fungal TNT-NADases

Next, we scrutinized the occurrence and diversification of the TNT-containing NADases in fungi by conducting a comprehensive phylogenetic analysis within this kingdom (Figure 3a). All identified NADases belong to the Ascomycota, Basidiomycota or Mucoromycota divisions (Table S1). Eurotiomycetes and Sordariomycetes classes account for the majority of the fungal NADases, with only a minority of species found in the Leotiomycetes, Lecanoromycetes, Agaricomycetes, Pucciniomycotina, Dothideomycetes, Morteriellomycotina and Mucoromycotina. The sequences included in the phylogenetic tree (Figure 3a) cluster in six readily discernible clades (marked I-VI; clade assignments are based on an extended phylogenetic tree including 460 sequences, see GitHub). The inspection of the sequences revealed consistent differences at the N- and C-terminal regions of the predicted proteins, following the branches of the tree (Figure 3a). The residues previously identified to form a Ca^{2+} binding motif important for dimer stabilization in *Af*NADase (Asp219, Glu220 and Glu223) (Ferrario et al., 2023; Strømland et al., 2021) are conserved only in the Eurotiomycetes class (Clade IV; Figure 3a, highlighted in red). In the clade containing sequences from Sordariomycetes as well as Leotiomycetes, mostly Fusarium and Botrytis genus, respectively, we note the strong conservation of cysteine residues in both the N- and C-terminal region of the NADase (Clade I; Figure 3a, highlighted in green). Concurrently, some NADases of Sordariomycetes such as *Neurospora crassa* (Clade II) and Eurotiomycetes (Clade VI), together with other classes (present in Clades II-III-V) do not exhibit

FIGURE 2 Evolutionary distribution of the TNT domain. (a) Sequence alignment of *Mtb*CpnT CTerm and *Af*NADase, with the structural features of both enzymes color-coded. *Mtb*CpnT CTerm NAD binding residues are identified by structural superimposition with *Af*NADase in complex with BAD (PDB 6YGG). (b) Distribution of TNT domain in the domains of life, and class spreading. Black columns represent the sum of species individuated in each kingdom. (c) Occurrence of IFT in different orders of bacteria. The black column represents the sum of species individuated. (d) Unrooted phylogenetic tree analysis showing species distribution of TNT-proteins. The evolutionary history was evaluated using maximum-likelihood method and LG model on MEGA 11. The tree is drawn to scale, with the branch length reflecting the number of substitutions per site. The taxon are colored based on fungal class, and are colored in black for bacterial sequences. The asterisks highlight the TNT-proteins further analyzed in the article (*Nc*NADase, *Af*NADase, *Fo*NADase1 and *Mtb*CpnT). Clades assignments are shown in roman numbers and are based on an extended phylogenetic tree of 460 TNT-proteins (see GitHub link). Clade S represents the bacterial sequences that are mixed with Clade VI sequences in the 460 sequences phylogenetic analysis (GitHub link).
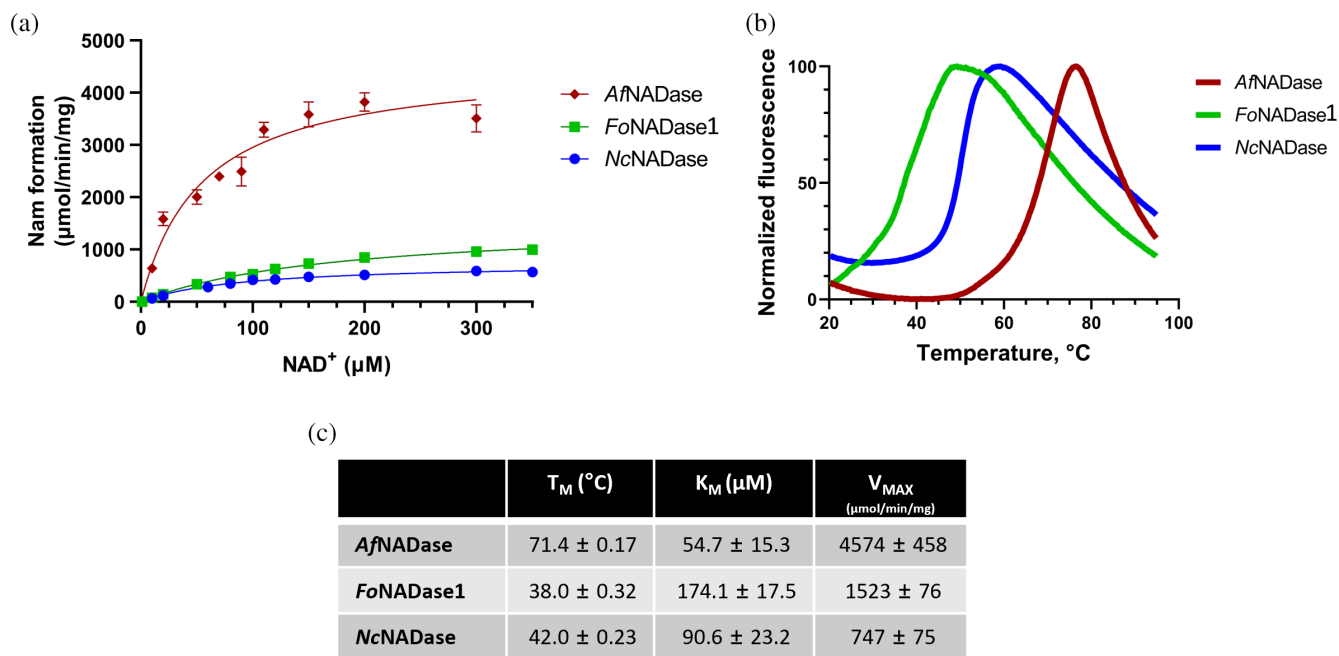
(a)

(b)
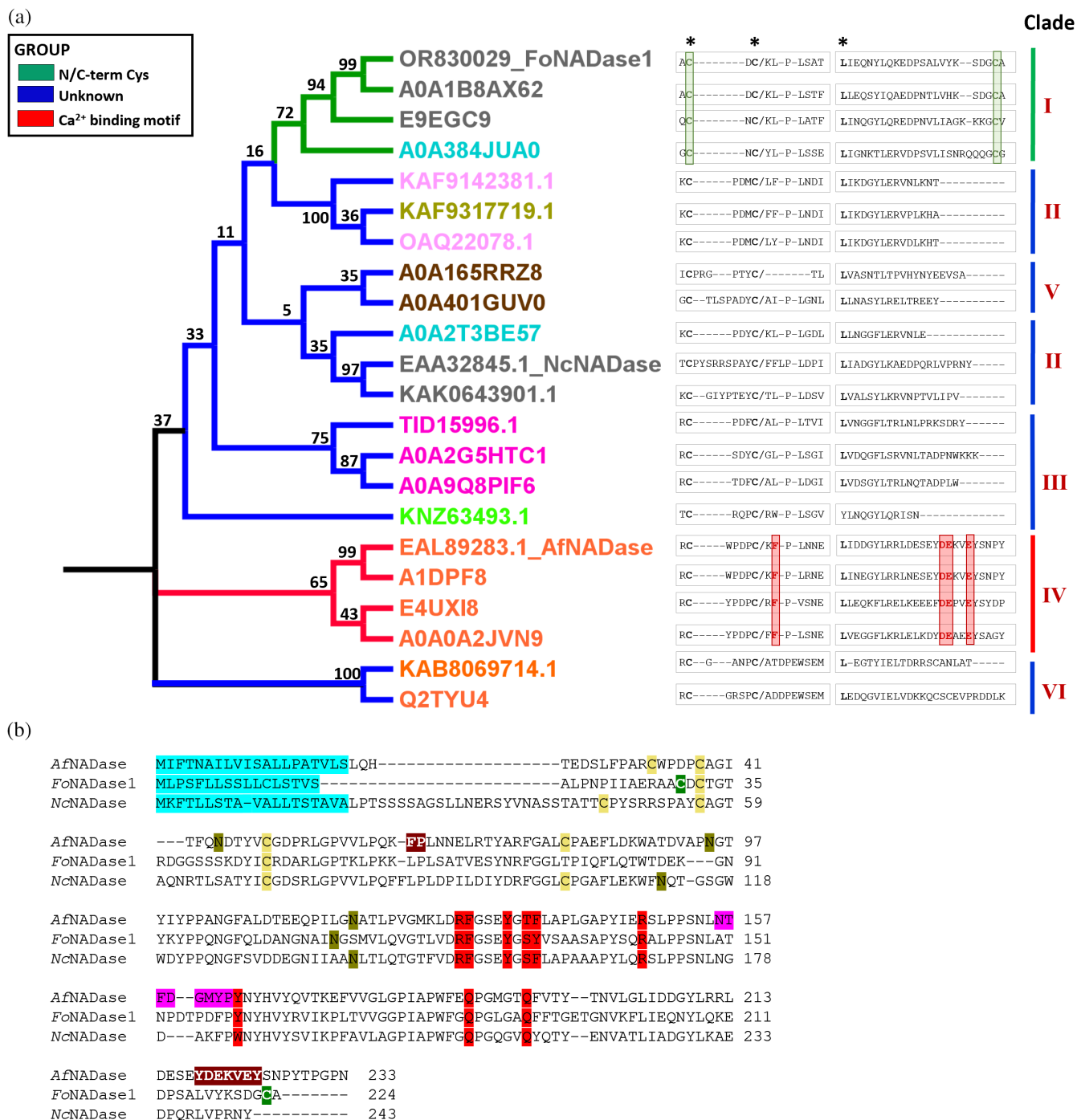
FIGURE 3 Phylogenetic and sequence analysis of fungal TNT NADases. (a) Phylogenetic distribution and sequence characteristics of fungal TNT-containing NADases. The phylogenetic tree has been built using maximum-likelihood method and LG model using MEGA 11. The results have been visualized via cladogram to highlight the branching pattern. The color pattern of the taxa follows what is shown in Figure 2d, while the clades are colored based of N/C terminal characteristics and divided into three different groups (red, green, blue). Residues marked with * are conserved in all sequences. (b) Sequence alignment of *Af-Fo-Nc* NADases with highlighted in color the features of each enzyme (cyan: Signal peptide, yellow: intramolecular disulfide bridges, red: NAD binding residues, magenta: ^{156}NTFDGMYPY^{162} loop, olive: glycosylation sites, brown (*Af*NADase) and green (*Fo*NADase1): clade specific conserved residues).

group specific conserved residues at the N- and C-termini (Figure 3a, highlighted in blue). As previously introduced, the crystal structures of *Af*NADase reveal that the two protomers within the homodimer form a head-to-tail arrangement, connecting the N- and C-terminus of the

protein. Hence, the variations observed in these regions suggest a clade specific diversification of homodimer stabilization, discernible in three different groups.

F. oxysporum f.sp. *cubense* race 1 has two NADase isoforms encoded by the genes *nadA1* (*Fo*NADase1,

(a)

(b)

(c)

	T_M (°C)	K_M (μM)	V_{MAX} (μmol/min/mg)
*Af*NADase	71.4 ± 0.17	54.7 ± 15.3	4574 ± 458
*Fo*NADase1	38.0 ± 0.32	174.1 ± 17.5	1523 ± 76
*Nc*NADase	42.0 ± 0.23	90.6 ± 23.2	747 ± 75

FIGURE 4 Biochemical characterization of *Af*NADase, *Fo*NADase1 and *Nc*NADase. (a) Kinetic analysis of *Af-Fo-Nc* NADases, using a fluorometric assay and etheno-NAD$^+$ as substrate. Results show the average ± SD of two independent experiments performed in technical triplicates. (b) Melting curves obtained via differential scanning fluorimetry experiment on *Af-Fo-Nc* NADases. Fluorescence was normalized to the maximum signal of the protein to allow relative comparison ($n = 3$). (c) Table summarizing the kinetic parameters and melting temperature of each characterized NADase.

OR830029) and *nadA2* (*Fo*NADase2, OR830030), sequences included in the phylogenetic tree including 460 sequences (see GitHub link). This duplication was identified primarily in Fusarium species, with both sequences clustering within the same clade (Clade I, see 460 sequences tree on GitHub), hinting at a recent gene duplication event. The presence of Eurotiomycetes in both Clade IV and VI is intriguing. Thus, Eurotiomycetes present in Clade VI do not possess the residues involved in Ca^{2+} binding motif formation but, notably, are associated with bacterial TNT-proteins from Clade S.

Figure 3b shows a sequence alignment of representatives of each of the three fungal NADase groups, including those from *A. fumigatus* (*Af*NADase), *N. crassa* (*Nc*NADase) and *F. oxysporum* f.sp. *cubense* race 1 (*Fo*NADase1). As can be noted, the central TNT domain sequence is well conserved across all fungal NADases, whereas the N-termini (excluding the signal peptides) and the C-termini are highly diverse.

2.3 | Biochemical proprieties of fungal TNT-NADases are governed by their N and C-termini

We earlier demonstrated that the C-terminus of *Af*NADase is critical for both enzymatic activity and dimer stability (Ferrario et al., 2023). Therefore, we proceeded to characterize the representative NADases of each of the

three fungal groups (*Af*NADase, *Fo*NADase1, *Nc*NADase; Figure 3a) with regard to their biochemical and structural properties. The NADases were expressed in Sf9 cells using a baculovirus system followed by purification as described in the methods section. Determination of the melting temperatures (T_M) and kinetic parameters of the purified enzymes (Figure 4a–c) revealed that *Af*NADase has the highest T_M (71.4 ± 0.17°C), followed by *Nc*NADase (T_M: 42.0 ± 0.23°C) and *Fo*NADase1 ($T_M = 38.0 ± 0.32$°C) (Figure 4b). Likewise, *Af*NADase has the highest activity (V_{max}: 4574 ± 458 μmol/min/mg; K_M: 54.7 ± 15.3 μM) compared to *Nc*NADase (V_{max}: 747 ± 75 μmol/min/mg, K_M: 90.6 ± 23.2 μM) and *Fo*NADase1 (V_{max}: 1523 ± 76 μmol/min/mg K_M: 174.1 ± 17.5 μM) under the assay conditions (Figure 4a,c).

2.4 | *Fo*NADase1 stabilizes homodimer conformation via intermolecular disulfide bonds

Despite having a high degree of sequence identity with *Af*NADase, *Fo*NADase1 exhibited markedly different kinetic and thermodynamic properties (Figure 4a-c) suggesting that the sequence variations, such as the lack of residues forming the C-terminal Ca^{2+} binding motif, may have a significant impact on the enzymatic proprieties. To identify the structural consequences caused by these
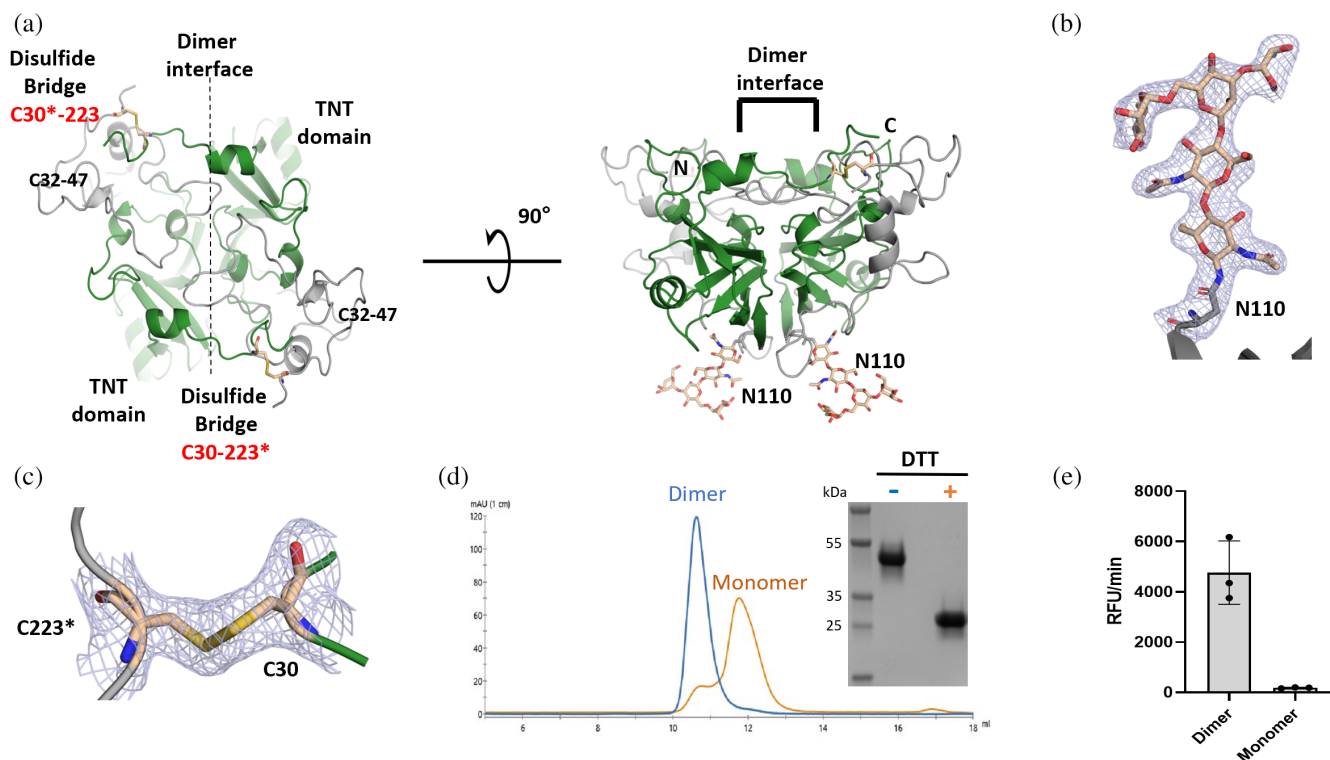
FIGURE 5 Crystal structure of *Fo*NADase1 and disulfide bonds mediated homodimer stabilization. (a) Cartoon representation of dimeric *Fo*NADase1. The TNT domain of each protomer is colored green, while the thumb domain is gray. The residues involved in the intermolecular disulfide bridge are shown in stick representation and colored in light brown. The glycosylated asparagines are given at the bottom of the structure in stick representation. C- and N-terminus of a protomer are indicated with "C" and "N." (b) 2Fo-Fc electron density map contoured at σ = 1 of observed glycosylation of Asn110 shown in stick representation. (c) 2Fo-Fc electron density map contoured at σ = 1 with cartoon-stick representation of the intermolecular disulfide bridge between Cys223* and Cys30, with the two protomers colored in green and gray respectively. (d) Superimposition of size-exclusion chromatography (SEC) chromatograms of *Fo*NADase1 without (blue) and with DTT-treatment (orange). Inset: SDS-PAGE of *Fo*NADase1 with and without added DTT confirms the reduction of the disulfide bond. (e) Enzymatic activity of *Fo*NADase1 in dimeric and monomeric state. The protein samples obtained from the experiment shown in Figure 4d were collected, quantified, and utilized for the analysis (*n* = 3).

variations we solved the crystal structure of *Fo*NADase1 (Figure 5a; Table I). We observed only one protomer in the asymmetric unit (ASU), although the biological assembly of the protein is a homodimer. The dimer is therefore completed by a symmetry-related molecule within the unit cell (residues from symmetry-related amino acid chain, constituting the complementary protomer, are from here on marked with a *) (Figure 5a and Table 1). The overall protein fold resembles *Af*NADase (PDB 6YGE), with two protomers forming a homodimer. Each protomer is formed by a thumb domain, and a TNT-like palm domain containing the active site of the enzyme. The thumb domain is stabilized by an intramolecular disulfide bridge between a Cys32 and Cys47, and as predicted, has one glycosylation site per protomer on residue Asn110 (Figure 5b). As suggested by the sequence analysis (Figure 3a,b), *Fo*NADase1 lacks the C-terminal portion of *Af*NADase constituting the Ca^{2+} binding motif involved in dimer stabilization and catalysis regulation

(Ferrario et al., 2023). Indeed, the dimerization interface of the Fusarium enzyme reassembles the one seen in the Ca^{2+}-depleted form of the *Af*NADase (PDB 8PMR; Ferrario et al., 2023) with loop–loop interactions between protomers. Interestingly, in *Fo*NADase1 the dimerization is stabilized via two intermolecular disulfide bridges between Cys30 and Cys223*, and Cys30* and Cys223, covalently linking the two protomers (Figure 5a,c). Clear electron density was observed for the disulfide bonds between the cysteines (Figure 5c). To further confirm the formation of this covalent bond and its role in homodimer stabilization, the purified enzyme was incubated with the reducing agent dithiothreitol (DTT). The treatment resulted in almost complete reduction of the disulfide bonds, allowing separation of the dimer into the monomer during size exclusion chromatography (Figure 5d). Importantly, the monomeric fraction isolated by size-exclusion chromatography did not show enzymatic activity towards ε-NAD (Figure 5e). These

observations suggest that the N-/C-terminal disulfide bonds are crucial for dimerization and for the catalytic activity of the NADase enzyme.

2.5 | AlphaFold2 predicted structure of *Nc*NADase highlights the presence of hydrogen-bond-based homodimer stabilization

Given the importance of the N- and C-terminal parts of NADases from *A. fumigatus* and *F. oxysporum* representing the clades I and IV to sustain a functional enzyme, we wondered how dimer stabilization is achieved in other clades (Figure 3a, Clade II and by extension III, V, VI). To elucidate this question, *Nc*NADase, belonging to the clade II, was used as the representative of the fungal TNT protein group highlighted in blue (Figure 3a). Unfortunately, crystallization of native *Nc*NADase proved unsuccessful, but we were able to solve the crystal structure for a construct in which the *Nc*NADase C-terminus was replaced with C-terminal amino acids of the *Af*NADase (termed *Nc*NADase *Af* $^{\text{C-Term}}$). The obtained dimeric structure enabled us to determine the core fold of *Nc*NADase (PDB 8R17; Figure S1 and Table 1), which was comparable to that of *Fo*NADase1 (RMSD of 1.391 over 273 C$^{\alpha}$) and *Af*NADase (RMSD of 1.811Å over 278 C$^{\alpha}$). To gain insights into the assembly of the N- and C-termini of the native *Nc*NADase dimer, we used AlphaFold2 (Jumper et al., 2021; Mirdita et al., 2022) to generate a structural model. The software was provided with *Af*NADase (PDB 6YGE), *Af*NADase$^{\text{D219A/E220A}}$ (PDB 8PMR), *Fo*NADase1 (PDB 8R15), and *Nc*NADase *Af* $^{\text{C-Term}}$ (PDB 8R17) structures for the modeling. The predicted AlphaFold-model, *Nc*NADase$_{\text{AFold}}$, represented a homodimer structure with an overall protein fold similar to that of the other fungal NADase structures (PDBs 6YGE, 8PMR, 8PMS and 8R15; Figure 6a, S2). As for *Fo*NADase1, the dimerization interface of *Nc*NADase$_{\text{AFold}}$ presents loop-to-loop interactions within the two protomers. Unlike *Af*NADase and *Fo*NADase1, the N- and C-terminal regions do not have any readily discernible prominent features that could mediate stabilization of the homodimer. Instead, these regions form, in the *Nc*NADase$_{\text{AFold}}$ model, an extended network of hydrogen bonds, between the N-terminal and C-terminal residues of the protein, specifically Asn32/Tyr243[#] and Arg34/Asn242[#] (residues marked with [#] refer to the complementary protomer) (Figure 6b,c). Due to the absence of distinct N- and C- terminal motifs in the clades III, V and VI, we can only assume a similar stabilization mode suggested for clade II, based on the structural study of *Nc*NADase.

**TABLE 1** Data collection and refinement statistics.

	*Fo*NADase1, 8R15	*Nc*NADase *Af* $^{\text{C-Term}}$, 8R17
Data collection		
Wavelength	1.033	1.033
Resolution range	45.13–2.40 (2.51–2.4)	43.98–2.30 (2.382–2.30)
Space group	P 3$_2$ 2 1	P 4$_3$ 2$_1$ 2
Unit cell	83.06 83.06 57.964 90 90,120	83.756 83.756103.22 90 90 90
Multiplicity	3.6 (3.3)	8.7 (8.4)
Completeness (%)	89.78 (60.52)[a]	99.90 (99.88)
Mean I/sigma(I)	8.09 (1.23)	22.09 (1.10)
Wilson B-factor	43.23	75.33
R$_{\text{merge}}$	0.113 (0.917)	0.0477 (2.012)
CC1/2	0.994 (0.396)	0.999 (0.433)
Refinement		
No of unique reflections used for refinement / reflections for R-free	8351/427	16898/867
R-work/ R-free	0.199/0.237	0.247/0.262
Number atoms		
Protein	1535	1463
Ligand	67	84
Solvent	72	23
RMS(bonds)	0.004	0.009
RMS(angles)	0.72	0.99
Ramachandran favored (%)	97.98	95.11
Ramachandran allowed (%)	2.02	4.35
Ramachandran outliers (%)	0	0.54
Average B-factor		
Protein	46.11	83.37
Ligand	71.06	104.19
Solvent	45.57	73.02

Note: Statistics for the highest-resolution shell are shown in parentheses.
[a]The completeness of the data was under 90% only for the highest resolution cell. This was due to using diffraction on from the corners of the detector.

2.6 | Head-to-tail stabilization strategies effectively decrease dimer interface solvation energy gain

Apart from the different strategies utilized by *Af-Fo-Nc*NADases to promote homodimer stabilization, the other most evident difference between the proteins is the organization of the dimerization interface
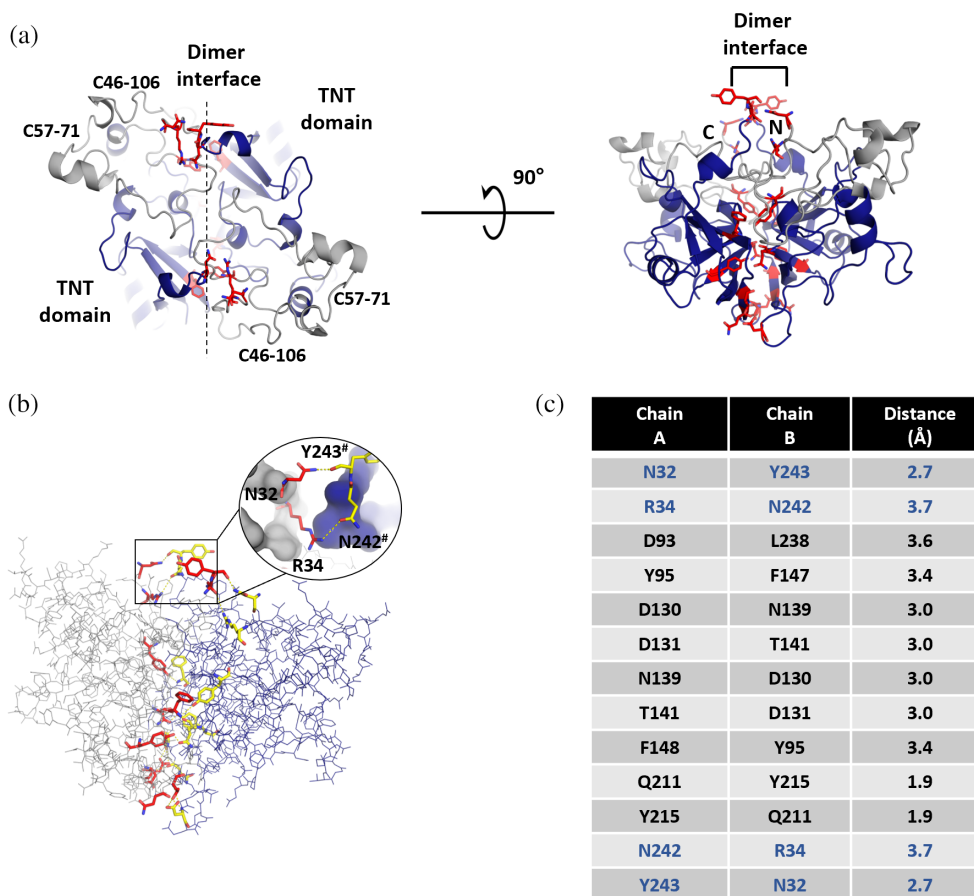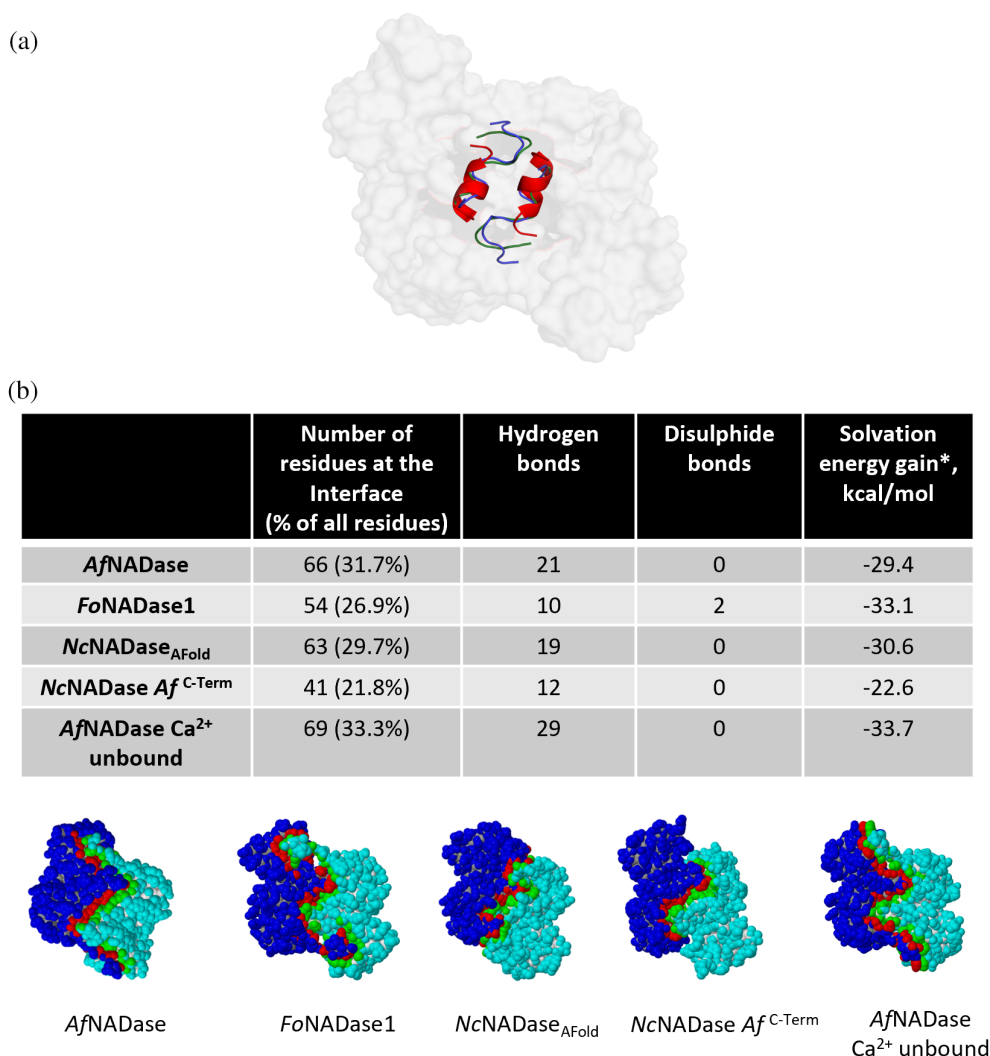
FIGURE 6 AlphaFold2 model of *Nc*NADase shows hydrogen bond-based homodimer stabilization. (a) Left panel, cartoon representation of *Nc*NADase_AFold. The palm domain of each protomer is colored in blue, while the thumb domain in gray. The C/N-termini residues involved in the polar interaction within protomers are shown in stick representation and colored in red. Right panel, x-axis 90° rotation of the dimer. (b) Representation of *Nc*NADase structure model with the two protomers highlighted in lines, and the residues involved in hydrogen bond-based protomers interface interaction in red and yellow sticks respectively to each protomer. The zoom-in panel shows the hydrogen bonds between Asn32/Tyr243[#] and Arg34/Asn242[#]. (c) The table lists the residues involved in hydrogen bond-based protomers interaction and respective bond length.

Table (c):

Chain A	Chain B	Distance (Å)
N32	Y243	2.7
R34	N242	3.7
D93	L238	3.6
Y95	F147	3.4
D130	N139	3.0
D131	T141	3.0
N139	D130	3.0
T141	D131	3.0
F148	Y95	3.4
Q211	Y215	1.9
Y215	Q211	1.9
N242	R34	3.7
Y243	N32	2.7

(Figure 7a). While *Af*NADase presents part of the dimer interface formed by two α-helices (PDB 6YGE), both *Fo*NADase1 and *Nc*NADase (both *Nc*NADase *Af*^C-Term and *Nc*NADase_AFold) display a mode of interaction between their two constituent protomers based on loop–loop interactions. This last conformation was also observed in the Ca²⁺ depleted conformation of *Af*NADase (PDB 8PMR; Ferrario et al., 2023). The comparative analysis of the dimer interface of the three NADases conducted through PDBePISA (Protein, Interfaces, Structures and Assemblies, https://www.ebi.ac.uk/pdbe/pisa/) (Krissinel & Henrick, 2007) shows a comparable number of hydrogen bonds in the *Af*NADase and *Nc*NADase dimers (Figure 7b). *Fo*NADase1 has a lower hydrogen bond content but compensates with the presence of two disulfide bonds stabilizing the dimerization interface. *Fo*NADase1 also shows the lowest solvation energy gain (ΔiG) of −33.1 kcal/mol, followed by *Af*NADase Ca²⁺

unbound (−33.7 kcal/mol), *Nc*NADase (−30.6 kcal/mol) and *Af*NADase (−29.4 kcal/mol). Intriguingly, *Af*NADase with Ca²⁺ depleted, establishes eight additional hydrogen bonds and presents a higher solvation energy gain compared to *Af*NADase, caused by differences in conformation of the C-terminus. Despite that, the contribution of the Ca²⁺ ion on *Af*NADase homodimer stabilization is not taken into account in PISA and therefore the ΔiG is expected to be lower, in line with what is shown in Figure 4b.

2.7 | *Fo*NADase1 active site reassembles *Af*NADase product release conformation

The residues involved in the substrate binding differ slightly between fungal NADases but they maintain the same physicochemical properties, as can be seen from

(a)

(b)

	Number of residues at the Interface (% of all residues)	Hydrogen bonds	Disulphide bonds	Solvation energy gain*, kcal/mol
*Af*NADase	66 (31.7%)	21	0	-29.4
*Fo*NADase1	54 (26.9%)	10	2	-33.1
*Nc*NADase_AFold	63 (29.7%)	19	0	-30.6
*Nc*NADase Af C-Term	41 (21.8%)	12	0	-22.6
*Af*NADase Ca²⁺ unbound	69 (33.3%)	29	0	-33.7

AfNADase   FoNADase1   NcNADase_AFold   NcNADase Af C-Term   AfNADase Ca²⁺ unbound
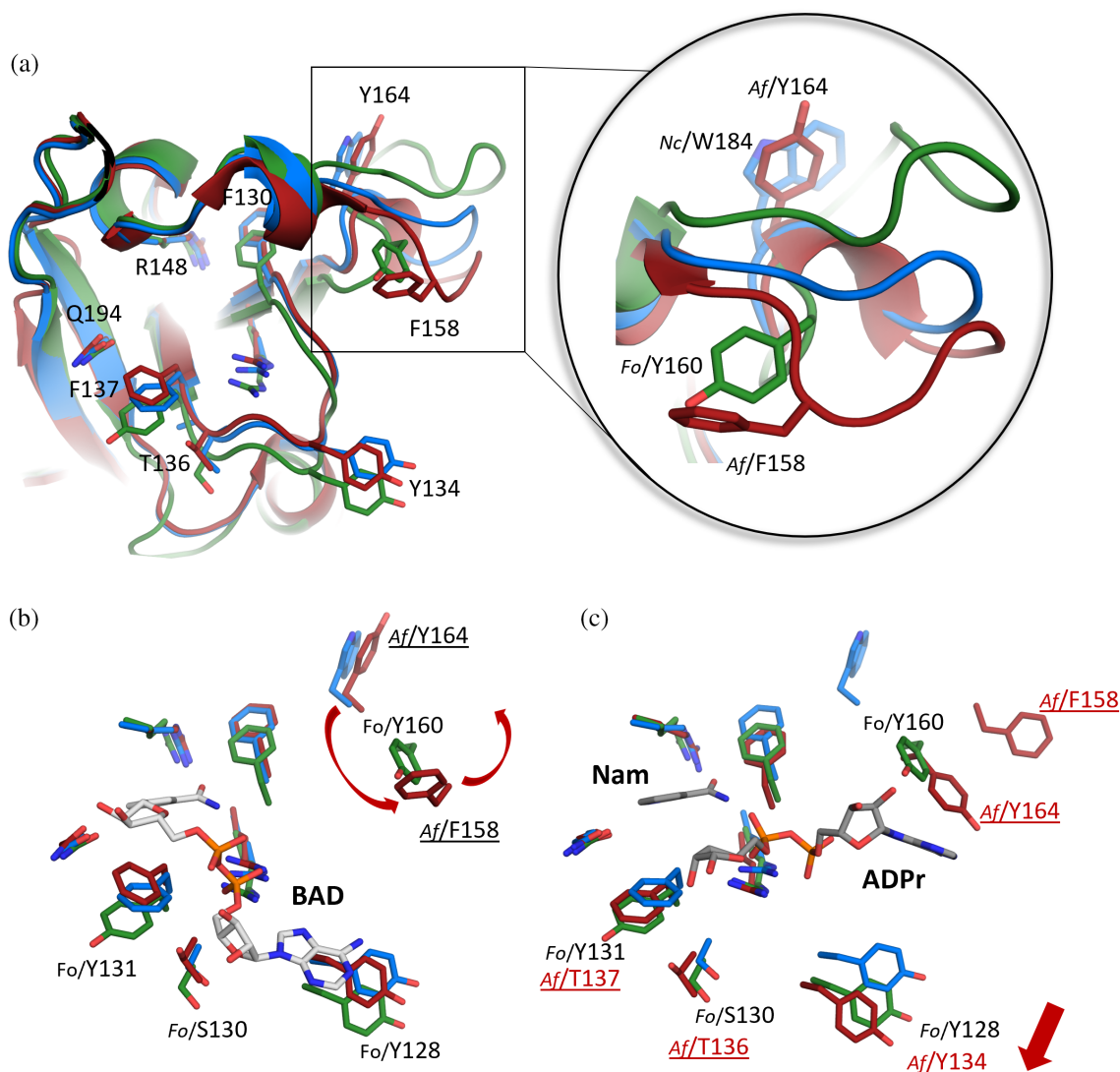
FIGURE 7 Comparison of the dimerization interface of *Af-Fo-Nc*NADases. (a) Superimposition of *Af*NADase (red, PDB 6YGE), *Fo*NADase1 (green, PDB 8R15), and *Nc*NADase_AFold (blue) structures, with emphasis on the different conformations of the dimer interface between the three enzymes. (b) PDBePISA evaluation of structural and chemical proprieties of the dimerization interface. The table shows the summary of the number of interacting residues at the dimerization interface, the type of chemical bond, and solvation energy gain of each NADase. Shown below are the respective NADase structures; blue and green spheres correspond to the residues present at the dimerization interface. *Solvation energy gain (ΔiG): indicates the solvation-free energy gain upon formation of the interface, in kcal/M. The value is calculated as difference in total solvation energies of isolated and interfacing structures. Negative ΔiG corresponds to hydrophobic interfaces, or positive protein affinity. This value does not include the effect of satisfied hydrogen bonds and salt bridges across the interface.

the sequence alignment (Figure 3b). Further, the structural comparison of the *Af*NADase (PDB 6YGE), *Fo*NADase1 (PDB 8R15) and *Nc*NADase_AFold confirms the similar arrangement of the active site (Figure 8a). In Strømland et al. the active site of *Af*NADase was observed in same conformation regardless of the state of the enzyme (apo, substrate analogue- and reaction products-bound state) (Strømland et al., 2021). Changes in the catalytic site conformation were only found in the Ca-depleted structure of *Af*NADase (PDB 8PMR) (Ferrario et al., 2023) where the comformation was more open in one of the observed dimers representing a possible

"product release conformation." The active site conformation of *Nc*NADase_AFold corresponds extremely well with apo *Af*NADase (Figure 8b). Whereas the active site for *Fo*NADase1 appears to be more open and the NAD-binding residues Tyr128, Ser130, and Tyr131 are shifted outwards approximately 2 Å when compared to *Af*NADase (Figure 8b).

The region where the loop ¹⁵⁶NTFDGMYPY¹⁶⁴ is located in *Af*NADase, shows several conformational variations between different fungal NADases. The *Af*/Phe158, residue that is interacting with the adenine group of ADPr (PDB 6YGF), is missing in both

FIGURE 8 Comparison of fungal NADases active site conformations. All figure panels show the structures from the same view orientation. (a) Structure superimposition of the catalytic pockets of *Af*NADase (red, PDB 6YGE), *Fo*NADase1 (green, PDB 8R15) and *Nc*NADase_AFold (blue). Residues involved in substrate/products binding are shown in stick representation. Residue labelling corresponds to *Af*NADase. Right panel: focus on the structural area presenting *Af*NADase ^{156}NTFDGMYPY^{164} loop involved in enzymatic activity regulation. (b) Superimposition of *Af*NADase BAD bound crystal structure (red, PDB 6YGG), *Fo*NADase1 (green, PDB 8R15) and *Nc*NADase_AFold (blue) catalytic pockets with residues involved in substrate binding shown in stick representation. The catalytic pocket of *Fo*NADase1 is in a slightly more open conformation, with a shift of circa 2 Å. Underlined residues mark the conformational switch of loop ^{156}NTFDGMYPY^{164} of *Af*NADase, affecting substrate-binding/product-release favoring conformations of the active site. Red arrows mark the movements of *Af*NADase residues to obtain the product release conformation. (c) Superimposition of *Af*NADase product release conformation (PDB 8PMR) with *Fo*NADase1 (green, PDB 8R15) and *Nc*NADase_AFold (blue) catalytic pockets. ADPr and Nam ligands are taken from *Af*NADase structure (PDB 6YGF). Residues involved in substrate binding are shown in stick representation. In this conformation *Af*NADase catalytic pocket shifts downward in a conformation similar to *Fo*NADase1. Residues underlined mark the conformational switch of loop ^{156}NTFDGMYPY^{164} of *Af*NADase, affecting the substrate-binding/product-release favoring conformations of the active site.

*Fo*NADase1 and *Nc*NADase_AFold (Figure 8a). When comparing the structures, the *Fo*/Tyr160 does not align with the *Af*/Tyr164 and the *Nc*/Trp184 (Figure 8a) as indicated by the sequence alignment (Figure 3b), instead, it falls in proximity with *Af*/Phe158 (Figure 8a). Interestingly, the comparison of the *Fo*NADase1 with the *Af*NADase Ca-depleted "product release-conformation" (PDB 8PMR)

(Ferrario et al., 2023), reveals a better overlay between the two structures (Figure 8c). Thus, the *Fo*NADase1 NAD-binding residues corresponds well with the "product release conformation" of *Af*NADase, and the *Fo*/Tyr160 is observed in a similar conformation as the Tyr164 after the conformational rearrangement of the loop ^{156}NTFDGMYPY^{164} (Figure 8c). The open active

site conformation of *Fo*NADase1 explains the higher measured K_M and lower V_{MAX} compared to wild type *Af*NADase (Figure 4a,c).

3 | DISCUSSION

The present study has established the phylogenetic distribution of TNT domain containing proteins (TNT-proteins) and unique structural and functional properties of representatives in fungi. The homology search across all domains of life shows a rather limited occurrence of TNT-proteins, confined to bacteria and fungi. Even within these domains, the presence of TNT-proteins is restricted to specific phyla (bacteria) and divisions (fungi). Among the organisms carrying TNT domains we observed a close evolutionary relationship between Clade S and Clade VI, which includes both bacterial and fungal species. In addition, our phylogenetic analysis reflected a distribution of TNT-proteins not consistent with the evolutionary relationship of their fungal classes (Clade II, Figure 2d). Together these data suggest that TNT-domains may be exchanged via intra- and inter-kingdom horizontal gene transfer, a mechanism reported to be involved in the transfer of virulence genes in microbes (Lee et al., 2022; Xu et al., 2023). In this regard, it is interesting to note that the TNT-proteins evolved independently from other NAD glycohydrolases both genetically and functionally. The TNT domain uses a unique catalytic mechanism to cleave NAD into ADP-ribose and nicotinamide (Strømland et al., 2021; Sun et al., 2015). This mechanism is different from that of other known NAD glycohydrolases, because it does not enable the formation of cyclic ADP-ribose or a base-exchange reaction. These reactions have been established, for example, for TIR domain proteins (Sasaki et al., 2020) and enzymes related to the *Aplysia californica* ADP-ribosyl cyclase such as CD38 (Howard et al., 1993). These NADases may have a function in virulence in some bacteria (Ogura et al., 2020; Vanden Broeck et al., 2007), but their catalytic versatility has been tuned in higher organisms to mediate sophisticated regulatory functions, such as calcium signaling by cADPR (Lee, 2001). That is, unlike other families of NAD glycohydrolases, the enzymatic activity of TNT-proteins in bacteria and fungi has the sole function of hydrolytic NAD cleavage. The absence of TNT-proteins in higher organisms suggests that the evolutionary advantage gained by this trait is limited to microorganisms. Given the destructive role of NADase activity in the mechanism of action of the *Mtb*TNT as a toxin (Sun et al., 2015), it seems plausible that the NADase of other TNT-proteins might also play a role in infection processes or microbial

warfare. In this context it is of interest that, in plants, extracellular NAD(P) appears to be an important component of antibacterial defense (Alferez et al., 2018; Li et al., 2021; Wang, 2019). It was proposed that leakage of NAD into the extracellular environment is associated with cell damage and recognized as a damage associated molecular pattern (DAMP) by adjacent cells which, in defense, induces a systemic acquired resistance response (SAR). Importantly, the presence of NADase activity in the extracellular environment increases the susceptibility to infection in plants (Zhang & Mou, 2012). In principle, TNT ectoNADases of both bacterial and fungal plant pathogens might contribute to virulence by exploiting such a mechanism. However, this remains to be investigated. Similarly, studies support a possible role of eNAD as antibacterial agent, able to reduce *Streptococcus pneumoniae* infection of human brachial epithelial cells (Klabunde et al., 2023) and stimulate immune response (Audrito et al., 2021).

The detailed exploration of TNT-proteins in fungi indicates a strong selective pressure towards stabilization of the head-to-tail homodimer assembly. Three rather different strategies have evolved to mediate tight interactions using the N- and C-termini of the protomers. Indeed, all three mechanisms utilized, namely Ca^{2+} binding in Clade IV, disulfide bonds in Clade I, and hydrogen bonds in Clades II, decrease the solvation energy gain (ΔiG) of the homodimers. The absence of clearly detectable patterns in the clades III, V and VI (Figure 3a) might suggest a similar stabilization to the one suggested for clade II, relying on intermolecular electrostatic interactions (e.g., hydrogen bonds). Electrostatic interactions can be formed by different combinations of amino acids, and losses/gains can occur more readily than for covalent bonds (e.g., disulfide bonds). Hence, pinpointing the residues involved in NADase homodimer stabilization is challenging and may require case by case experimental determination. Such information is critical, because formation and maintenance of a homodimeric structure is crucial for enzymatic activity as demonstrated by the nearly complete loss of catalytic activity following dissociation of the *Fo*NADase1 dimer by reducing agents (Figure 5d,e). *Af*NADase exhibits both higher affinity and catalytic rate compared to the other two fungal enzymes studied. The high catalytic efficiency of the *Af*NADase has previously been associated with long-range conformational changes, mediated by the [156]NTFDGMYPY[164] loop, which influences the active site of the enzyme upon Ca^{2+} binding and release (Ferrario et al., 2023). The mechanisms employed to stabilize *Fo*NADase1 and *Nc*NADase homodimers appear less likely to be able to contribute to changes in the active site. Notably, the active site of *Fo*NADase1 closely aligns with the Ca^{2+}-

unbound conformation of *Af*NADase (PDB 8PMR), a conformation that favors product release over substrate binding due to the wider conformation of NAD binding residues (Figure 8b) and the additional π-π interactions between *Fo*/Tyr160 and the adenosine ring of ADPr (Figure 8c). In contrast, the active site configuration of *Nc*NADase aligns well with the Ca^{2+}-bound/substrate binding favoring conformation of *Af*NADase (PDB 6YGE) and is distinguished by its absence of aromatic residues capable of interacting with ADPr, further substantiating its preference for substrate binding over product release as also reflected by its kinetic parameters (Figure 4a,c).

It is interesting to note though that all three modes of dimer stabilization are reversible. For example, reversible calcium binding in the *Af*NADase may be part of a catalytic cycle, since the changes evoked by calcium binding are transmitted to the catalytic site to enhance activity (Ferrario et al., 2023). It is conceivable that a similar conformational flexibility could be achieved through disulfide-sulfhydryl interchange in *Fo*NADase1, although this would require the presence of redox-active SH groups in close vicinity of the N- and C-termini, possibly provided by additional factors present on the fungal surface (Iozzi et al., 2011; Karimi et al., 2016). Likewise, a rearrangement of hydrogen bonds in the *Nc*NADase during the catalytic cycle could result in structural changes in the active site to promote catalysis.

Overall, our study has established that TNT-proteins are exclusively found in bacteria and fungi. This observation indicates that the biological function of this unique type of NADases is related to the specific life forms of these microorganisms. The fact that at least the fungal NADases are active on the outer surface suggests that their role is related to the interaction with other organisms in their environment. Whether this may be associated with infection mechanisms as known for the *Mtb*TNT remains to be elucidated. Our structural investigations have revealed an unexpectedly stringent requirement for dimer stabilization in these fungal proteins. According to our analyses, dimerization is important to enable robust NADase activity. However, we cannot rule out the possibility that this stabilization is important to maintain a functional state in the extracellular environment.

4 | CONCLUSIONS

This investigation elucidated the evolutionary trajectory of fungal ecto TNT-NADases, uncovering selective pressure promoting the homodimer stabilization via C-terminal/N-terminal intermolecular interactions, and simultaneous regulation of the active site conformation

of these enzymes. Extracellular NAD (eNAD) is rarely available, given its pivotal role in cellular energy metabolism and signaling. Therefore, the biological role of these enzymes remains obscure. One of the reported functions of eNAD is its role as damage-associated molecular pattern (DAMP) in plants, triggering immune response of adjacent cells upon pathogen invasion. In this context, the presence of ectoNADases, which can efficiently cleave and attenuate NAD signaling, may constitute a strategic advantage for host infection and evolutionary success. Hence, it is important to investigate the role of fungal TNT NADases in plant infections, particularly considering the significant economic and social consequences of fungal infections in agriculture, with *F. oxysporum* being one of the most concerning species (Arie, 2019; Dita et al., 2018).

5 | MATERIALS AND METHODS

5.1 | Expression and purification of *Af*NADase, *Fo*NADase1 and *Nc*NADase

The plasmids and the viruses encoding *Af*NADase were generated as described in Strømland et al., 2021. Genomic sequence of *nadA1* (encoding *Fo*NADase1) was amplified from genomic DNA obtained from CABI (UK; strain IMI 141109) using the following primer pairs: 5′-ggttgacattatctactcgaatggactgac-3′ and 5′-tgtcctttgttgttgagggcagc-3′. The obtained amplicons were cloned into a pJET1.2 cloning vector (Thermo Fisher Scientific) and sequence verified by Sanger sequencing. The predicted intron in the genomic sequence was removed by site directed mutagenesis. For recombinant protein expression the coding sequence of *Fo*NADase1 was amplified from the plasmid containing the gene and inserted in-frame with C-terminal HRV3C cleavage site and 6xHis-Tag in a pFastBackNKI-ORF-3C-His insect expression vector (NKI Protein facility, The Netherlands). *Nc*NADase was amplified from cDNA and inserted in-frame with a C-terminal HRV3C cleavage site and 6xHis-Tag in the pFastBacNKI-ORF-3C-His insect expression vector (NKI Protein facility, The Netherlands) as described in Strømland et al. (2021). DH10Bac *E. coli* cells were used for bacmid generation for *Nc*NADase, while EmBacY *E. coli* cells were used for *Fo*NADase1 and *Nc*NADase *Af* $^{C-Term}$. Bacmid preparation was performed following the protocol described by Bieniossek et al. (2008). Briefly, Sf9 cells (Invitrogen) in solution at a density of 0.5 million cells/mL were transfected with the bacmids of each enzyme of interest using the Cellfectin™ II Reagent (ThermoFischer Scientific), and the viruses were harvested after 7 days of incubation at 27°C at 300 rpm. As a next step, the recombinant primary viruses

(V1) were amplified by infecting a new batch of Sf9 cells to get a high-titer viral stock (V2). For protein expression Sf9 cells were grown in Sf-900 (Gibco™) medium and infected with V2 once at a density of 1.5 million cells/mL. Three days after insect cells grown arrest the cells were pelleted by centrifugation and the medium containing the secreted protein of interest was filtered using 0.22 μm filter (Merc Millipore). The enzyme of interest was purified by immobilized metal affinity chromatography (IMAC) using HisTrap™ excel (GE healthcare) column connected to an ÄKTA pure chromatography system (GE healthcare). The HisTrap column was washed with washing buffer (50 mM Tris–HCl pH 8.0, 300 mM NaCl) and the protein was eluted with elution buffer (50 mM Tris–HCl pH 8.0, 300 mM NaCl, 500 mM imidazole). The purified protein was concentrated using 10 kDa MWCO Amicon® Ultra Centrifugal filters (Merc Millipore), imidazole was removed from the solution using a PD-10 desalting column (Cytivia™) and desalting buffer (50 mM Tris–HCl pH 8.0, 300 mM NaCl). The sample was then incubated overnight with 3Case to cleave the 6xHis-tag, and after incubation the 3C protease was removed by batch His-affinity chromatography. Size exclusion chromatography (SEC) was performed as final purification step using a Superdex 200 16/60 HiLoad prepgrade column (GE Healthcare) using SEC buffer (50 mM Tris–HCl pH 8.0, 300 mM NaCl). All the purification steps were evaluated using SDS-PAGE. All purified enzymes yielded 5–10 mg of protein per liter of medium.

5.2 | Generation of *Nc*NADase *Af* ^{C-Term}

*Nc*NADase *Af* ^{C-Term} was generated using a PCR-based strategy by mutation of the parental plasmid generated by Strømland et al. (2021) using Q5 Site-Directed mutagenesis Kit (new England Biolabs Inc.). The primers were designed using NEB base exchanger web tool (New England Biolabs Inc.). *Nc*NADase *Af* ^{C-Term} was designed using the primers 5′-ATACTCGAATCCGTATAC-3′ and 5′-ACCACCTTCTCATCATACTC-3′ following manufactures protocol. The PCR product was inserted in-frame with a C-terminal C3 cleavage site and 6xHis-Tag in the pFastBacNKI-ORF-3C-His insect expression vector (NKI Protein Facility, The Netherlands).

5.3 | TNT/IFT blast search and phylogenetic trees generation

TNT blast search was performed using the TNT domain of *Af*NADase as query (115ILGNATLPVGMKLDRFGS EYGTFLAPLGAPYIERSLPPSNLNTFDGMYPYNYHVYQ VTKEFVVGLGPIAPWFEQPGMGTQFVTYTNVLGLIDD GYLRRLD213) against the reference protein (refseq_protein) database on NCBI and Pfam database. The search was selectively performed on each bacteria phylum and fungal class at the time via BLASP search with max target sequence of 1000 and expect threshold of 0.05. Sequences representative of each genus were selected from the BLAST search, collected and analyzed using MEGA11 (Tamura et al., 2021). Sequence alignment was performed using MUSCLE (Edgar, 2004). The phylogenetic trees were generated using Maximum-likelihood method (Felsenstein, 1981), Le_Gascuel_2008 model and automatically obtained initial tree for the heuristic search using NJ/BioNJ. The analysis was carried out using a site coverage of 95% with partial deletion option. Confidence levels were estimated using 500 cycles of the bootstrap method. Trees were visualized using FigTree (http://tree. bio.ed.ac.uk/software/figtree/).

IFT blast search was performed using the residues of *Mtb*IFT interacting with *Mtb*CpnT TNT (36NKGGEVRY FIDRLAGWYVITSSDRMSREGYEFAAASMSVIEKYLYG YFGGSVRSERELPAIRAPFQPEELMPEYSIGTMTFAGR QRDTLIDSSGTVVAITA137) and settings as reported before for the TNT blast search.

5.4 | Differential scanning fluorimetry (DSF) to determine T_M

Thermal denaturing was investigated to obtain the protein melting point, T_M. Denaturing profiles for the enzymes were analyzed using a light cycler 480 real time PCR (Roche) with excitation and emission wavelength of 472 and 572 nm, respectively. The assay was performed with 0.2 mg/mL protein concentration in phosphate-buffered saline (PBS) supplemented with 5x SYPRO Orange (Thermo) on 384-well plates with 20 μL sample volume. Data were analyzed using HTSDSF Explorer (Martin-Malpartida et al., 2022) and GraphPad Prism.

5.5 | Determination of *Af*NADase, *Fo*NADase1 and *Nc*NADase kinetics by fluorescence spectrophotometry

The kinetic characterization of the enzymes in study was conducted using a TECAN Spark® multimode plate reader, following the hydrolysis of a fluorescent NAD analog (etheno-NAD, excitation-emission wavelength 300–410 nm respectively) in 96 well black flat-bottom plates (Corning®) at 25°C. The kinetic measurement was conducted with 10 ng of enzyme and a substrate

concentration ranging from 1 to 500 μM in reaction buffer (50 mM sodium acetate pH 5.5, 150 mM NaCl, 500 μM $CaCl_2$) in a final volume of 100 μL. RFU were converted into moles using a calibration curve obtained from the complete conversion of different concentrations of etheno-NAD upon 2 h incubation with 100 ng of purified *Af*NADase. The kinetic parameters were calculated using GraphPad Prism 9.1.1 and plotted using the Michaelis–Menten equation.

5.6 | X-ray crystallography

Prior to screening for crystallization conditions, the enzymes were concentrated using Amicon Ultra centrifugal filter (Merck KGaA, Darmstadt, Germany) with a 10 kDa cut-off. Crystallization was performed using the vapor diffusion method with MRC SD2 sitting drop plates (Molecular Dimensions Limited, Rotherham, UK) and the pipetting was done using a Mosquito LCP crystallization robot (SPT LabTech, Melbourn, UK).

The initial screenings were carried out using commercial screens PACT premier, JSCG plus, and Mem-Gold at 20 and 8°C. For *Fo*NADase1 hits from the initial screenings were optimized and plates were incubated at 8°C. Crystals were observed after 1 week to a month from conditions containing 15%–20% (w/v) polyethylene glycol (PEG) 1500, 100 mM MIB buffer at pH varying from 5 to 7. For *Nc*NADase *Af* [C-Term] JSCG plus condition 2–36 (0.1 M Bis-Tris pH 5.5, 3.8 M NaCl) was optimized and plates were incubated at 20°C. Best crystals were produced when setting Bis-Tris buffer at pH 6.5.

*Fo*NADase1 crystals were cryoprotected by soaking in crystallization solution supplemented with 30% (v/v) PEG400, and for *Nc*NADase *Af* [C-Term] crystals were cryoprotected with 25% (v/v) glycerol prior to flash freezing in liquid N_2. Diffraction data were collected at 100 K using synchrotron radiation at the P11 beamline at PETRA III/DESY in Hamburg, Germany. Diffraction data were processed using XDS (Kabsch, 2010) and scaled using AIMLESS (Evans, 2013). Data collection and refinement parameters are presented in Table 1. The *Fo*NADase1 structure was determined using the molecular replacement phaser and the protomer from *Af*NADase (PDB 6YGE) as a search model, and for *Nc*NADase *Af* [C-Term] the *Fo*NADase1 was used as a search model. The structures were refined with phenix.refine (Afonine et al., 2012) in the PHENIX package (Liebschner et al., 2019) in alternating cycles with manual adjustment performed in Coot (Emsley & Cowtan, 2004). Figures and RMSD values were generated in PyMol (The PyMOL Molecular Graphics System, Version 2.0 Schrödinger, LLC).

5.7 | *Fo*NADase1 DTT treatment and oligomeric state evaluation

Purified *Fo*NADase1 was added with 10 mM DTT and incubated for 1 h on ice. The treated protein was loaded on a ÄKTA pure chromatography system (GE healthcare), connected to a size exclusion chromatography (SEC) column (Superdex 75 increase 10/300 GL, Cytiva). SEC was run using SEC buffer supplemented with DTT (50 mM Tris–HCl pH 8.0, 300 mM NaCl, 1 mM DTT). The DTT treatment was also analyzed using SDS-PAGE with non-reducing and normal (reducing) conditions. This was done by mixing the protein with SDS loading buffer either with or without DTT before heating the samples.

5.8 | AlphaFold 2 based *Neurospora crassa* NADase structure prediction

AlphaFold2 colab (Cramer, 2021; Mirdita et al., 2022) was utilized to generate a structural model of *Nc*NADase using as templates the .pdb structures of *Af*NADase (PDB 6YGE), *Fo*NADase1 (PDB 8R15) and *Nc*NADase *Af* [C-Term] (PDB 8R17). Ten models were generated and ranked by pLDDT, pTM and ipTM scores. The chosen model has the scores pLDDT: 81.1; pTM: 0.831; ipTM: 0.82 and was used as reference model of *Nc*NADase protein structure (*Nc*NADase[AFold]).

ACCESSION NUMBERS

The atomic coordinates included in the study have been deposited in the Protein Data Bank (PDB) with the following accession codes: *Fo*NADase1, 8R15 and *Nc*NADase *Af* [C-Term], 8R17. The genomic sequence of *Fusarium oxysporum f. sp. cubense* (race1) nadA1 and nadA2 were deposited in GenBank under the accession numbers OR830029 and OR830030, respectively.

AUTHOR CONTRIBUTIONS
Eugenio Ferrario: Conceptualization; investigation; writing – original draft; data curation. **Juha P. Kallio:** Investigation; data curation; writing – review and editing. **Mahdi Emdadi:** Investigation. **Øyvind Strømland:** Investigation; writing – review and editing. **Johannes G. M. Rack:** Writing – review and editing; data curation; funding acquisition. **Mathias Ziegler:** Funding acquisition; conceptualization; writing – review and editing.

CONFLICT OF INTEREST STATEMENT
The authors declare no competing interests.

DATA AVAILABILITY STATEMENT
NcNADase$_{AFold}$ structure (.pdb), sequence alignments (.mas) and phylogenetic trees (.nwk) presented in this article are available at the following link: https://github.com/UiBNAD/TNT_NADase

ORCID
Eugenio Ferrario https://orcid.org/0000-0001-6429-7980
Juha Pekka Kallio https://orcid.org/0000-0003-3092-4012
Mahdi Emdadi https://orcid.org/0009-0007-6612-6019
Øyvind Strømland https://orcid.org/0000-0003-2841-4638
Johannes G. M. Rack https://orcid.org/0000-0001-8341-6439
Mathias Ziegler https://orcid.org/0000-0001-6961-2396

REFERENCES
Afonine PV, Grosse-Kunstleve RW, Echols N, Headd JJ, Moriarty NW, Mustyakimov M, et al. Towards automated crystallographic structure refinement with phenix.refine. Acta Crystallogr D Biol Crystallogr. 2012;68:352–67.

Alferez FM, Gerberich KM, Li JL, Zhang Y, Graham JH, Mou Z. Exogenous nicotinamide adenine dinucleotide induces resistance to citrus canker in citrus. Front Plant Sci. 2018;9:1472.

Arie T. Fusarium diseases of cultivated plants, control, diagnosis, and molecular and genetic studies. J Pestic Sci. 2019;44:275–81.

Audrito V, Messana VG, Brandimarte L, Deaglio S. The extracellular NADome modulates immune responses. Front Immunol. 2021;12:704779.

Bieniossek C, Richmond TJ, Berger I. MultiBac: multigene baculovirus-based eukaryotic protein complex production. Curr Protoc Protein Sci. 2008; 51:5.20.1-5.20.26.

Choi J, Kim SH. A genome tree of life for the fungi kingdom. Proc Natl Acad Sci U S A. 2017;114:9391–6.

Cramer P. AlphaFold2 and the future of structural biology. Nat Struct Mol Biol. 2021;28:704–5.

Danilchanka O, Sun J, Pavlenok M, Maueroder C, Speer A, Siroy A, et al. An outer membrane channel protein of mycobacterium tuberculosis with exotoxin activity. Proc Natl Acad Sci U S A. 2014;111:6750–5.

Dita M, Barquero M, Heck D, Mizubuti ESG, Staver CP. Fusarium wilt of banana: current knowledge on epidemiology and research needs toward sustainable disease management. Front Plant Sci. 2018;9:1468.

Edgar RC. MUSCLE: multiple sequence alignment with high accuracy and high throughput. Nucleic Acids Res. 2004;32:1792–7.

Emsley P, Cowtan K. Coot: model-building tools for molecular graphics. Acta Crystallogr D Biol Crystallogr. 2004;60:2126–32.

Essuman K, Summers DW, Sasaki Y, Mao X, Yim AKY, DiAntonio A, et al. TIR domain proteins are an ancient family of NAD(+)-consuming enzymes. Curr Biol. 2018;28:421–30.e4.

Essuman K, Summers DW, Sasaki Y, Mao XR, DiAntonio A, Milbrandt J. The SARM1 toll/Interleukin-1 receptor domain possesses intrinsic NAD(+) cleavage activity that promotes pathological axonal degeneration. Neuron. 2017;93:1334–43.e5.

Evans PR. How good are my data and what is the resolution? Acta Crystallogr D Biol Crystallogr. 2013;69:1204–14.

Felsenstein J. Evolutionary trees from DNA sequences: a maximum likelihood approach. J Mol Evol. 1981;17:368–76.

Ferrario E, Kallio JP, Strømland Ø, Ziegler M. A novel calcium binding motif stabilizes and increases the activity of aspergillus fumigatus ecto-NADase. Biochemistry. 2023;62:3293–302.

Howard M, Grimaldi JC, Bazan JF, Lund FE, Santos-Argumedo L, Parkhouse RM, et al. Formation and hydrolysis of cyclic ADP-ribose catalyzed by lymphocyte antigen CD38. Science. 1993; 262:1056–9.

Iozzi MF, Helgaker T, Uggerud E. Influence of external force on properties and reactivity of disulfide bonds. J Phys Chem A. 2011;115:2308–15.

Jumper J, Evans R, Pritzel A, Green T, Figurnov M, Ronneberger O, et al. Highly accurate protein structure prediction with AlphaFold. Nature. 2021;596:583–9.

Kabsch W. XDS. Xds Acta Crystallogr D Biol Crystallogr. 2010;66: 125–32.

Karimi M, Ignasiak MT, Chan B, Croft AK, Radom L, Schiesser CH, et al. Reactivity of disulfide bonds is markedly affected by structure and environment: implications for protein modification and stability. Sci Rep. 2016;6:38572.

Klabunde B, Wesener A, Bertrams W, Beinborn I, Paczia N, Surmann K, et al. NAD+ metabolism is a key modulator of bacterial respiratory epithelial infections. Nat Commun. 2023; 14:5818.

Krissinel E, Henrick K. Inference of macromolecular assemblies from crystalline state. J Mol Biol. 2007;372:774–97.

Lee HC. Physiological functions of cyclic ADP-ribose and NAADP as calcium messengers. Annu Rev Pharmacol Toxicol. 2001;41: 317–45.

Lee IPA, Eldakar OT, Gogarten JP, Andam CP. Bacterial cooperation through horizontal gene transfer. Trends Ecol Evol. 2022; 37:223–32.

Li S, Ding H, Deng Y, Zhang J. Knockdown of quinolinate phosphoribosyltransferase results in decreased salicylic acid-mediated pathogen resistance in *Arabidopsis thaliana*. Int J Mol Sci. 2021;22:8484.

Liebschner D, Afonine PV, Baker ML, Bunkoczi G, Chen VB, Croll TI, et al. Macromolecular structure determination using X-rays, neutrons and electrons: recent developments in phenix. Acta Crystallogr D Struct Biol. 2019;75:861–77.

Marcet-Houben M, Gabaldon T. Acquisition of prokaryotic genes by fungal genomes. Trends Genet. 2010;26:5–8.

Martin-Malpartida P, Hausvik E, Underhaug J, Torner C, Martinez A, Macias MJ. HTSDSF explorer, a novel tool to analyze high-throughput DSF screenings. J Mol Biol. 2022;434:167372.

Mirdita M, Schutze K, Moriwaki Y, Heo L, Ovchinnikov S, Steinegger M. ColabFold: making protein folding accessible to all. Nat Methods. 2022;19:679–82.

Mittal E, Skowyra ML, Uwase G, Tinaztepe E, Mehra A, Koster S, et al. Mycobacterium tuberculosis type VII secretion system effectors differentially impact the ESCRT endomembrane damage response. MBio. 2018;9(6):e01765–18.

Ogura K, Yahiro K, Moss J. Cell death signaling pathway induced by Cholix toxin, a cytotoxin and eEF2 ADP-Ribosyltransferase produced by *Vibrio cholerae*. Toxins (Basel). 2020;13:13.

Pajuelo D, Tak U, Zhang L, Danilchanka O, Tischler AD, Niederweis M. Toxin secretion and trafficking by *Mycobacterium tuberculosis*. Nat Commun. 2021;12:6592.

Sasaki Y, Engber TM, Hughes RO, Figley MD, Wu T, Bosanac T, et al. cADPR is a gene dosage-sensitive biomarker of SARM1 activity in healthy, compromised, and degenerating axons. Exp Neurol. 2020;329:113252.

Simeone R, Bobard A, Lippmann J, Bitter W, Majlessi L, Brosch R, et al. Phagosomal rupture by *Mycobacterium tuberculosis* results in toxicity and host cell death. PLoS Pathog. 2012;8:e1002507.

Strømland O, Kallio JP, Pschibul A, Skoge RH, Harethardottir HM, Sverkeli LJ, et al. Author correction: discovery of fungal surface NADases predominantly present in pathogenic species. Nat Commun. 2021;12:2004.

Sun J, Siroy A, Lokareddy RK, Speer A, Doornbos KS, Cingolani G, et al. The tuberculosis necrotizing toxin kills macrophages by hydrolyzing NAD. Nat Struct Mol Biol. 2015;22:672–8.

Tamura K, Stecher G, Kumar S. MEGA11: molecular evolutionary genetics analysis version 11. Mol Biol Evol. 2021;38:3022–7.

Vanden Broeck D, Horvath C, De Wolf MJ. *Vibrio cholerae*: cholera toxin. Int J Biochem Cell Biol. 2007;39:1771–5.

Wang C. Extracellular pyridine nucleotides trigger plant systemic immunity through a lectin receptor kinase/BAK1 complex. Nat Commun. 2019;10:4810.

Xu Y, Liu Q, Meng G, Dong C. Horizontal gene transfer of Cccyt contributes to virulence of mycoparasite Calcarisporium cordycipiticola by interacting with a host heat shock protein. Int J Biol Macromol. 2023;242:124927.

Zhang X, Mou Z. Expression of the human NAD(P)-metabolizing ectoenzyme CD38 compromises systemic acquired resistance in Arabidopsis. Mol Plant Microbe Interact. 2012;25:1209–18.

SUPPORTING INFORMATION

Additional supporting information can be found online in the Supporting Information section at the end of this article.